JMEPEG (2010) 19:13–21
DOI: 10.1007/s11665-009-9391-0

1059-9495/$19.00

Numerical Simulation and Experimental Investigation of Residual Stresses in the Circumferential Butt GTAW of Incoloy 800H Pipes

H. Purmohamad, A. Kermanpur, and M. Shamanian

(Submitted July 10, 2008; in revised form January 12, 2009)

The residual stresses developed during the circumferential butt gas tungsten arc welding (GTAW) process of Incoloy 800H pipes were simulated using the finite element method. A decoupled thermostructural model was developed in three dimensions. The element birth and death technique was used for the addition of filler material in the weld pool. The Goldak double ellipsoidal model was used to simulate the distribution of arc heat during welding. The plastic behavior of the material was described by Von Mises yield function and the bilinear kinematics hardening was assumed. To validate the thermostructural model, both temperature and residual stress distributions within the pipes were measured using thermocouples and strain gages, respectively. Good agreements were found between the experimental and simulation results. The model was then used to predict distribution of residual stresses during the GTAW of Incoloy 800H pipes and to study effects of process parameters on the residual stresses.

Keywords finite element method, GTAW process, Incoloy 800H, residual stress

1. Introduction

Welding process is used in almost all industries such as fabrication of buildings, bridges, ships, oil-drilling rigs, pipelines, spaceships, nuclear reactors, and pressure vessels. One common problem associated with welding is the residual stresses and distortion. The highly localized transient temperature field in the welding processes causes nonuniform thermal expansion and contraction, resulting in residual stresses and distortion in the welded structures. High-tensile residual stresses in regions near the weld may promote brittle fracture, fatigue, and stress corrosion cracking. Therefore, control and accurate evaluation of weld residual stresses and distortion is a vital task in welding manufacturing (Ref 1).

Many experimental techniques have been used for measuring residual stresses in metals such as hole drilling and x-ray methods. All experimental methods, though, have at least two disadvantages. First, they are expensive to apply and their application usually requires special equipment and personnel that are not usually associated with structural engineering. Second, residual stresses can most often be measured at discrete locations on a weld, usually close to the weld surface. Obtaining a complete picture of residual stresses distribution in a typical weldment is practically impossible by experimental techniques (Ref 2).

H. Purmohamad, A. Kermanpur, and **M. Shamanian**, Department of Materials Engineering, Isfahan University of Technology, Isfahan 84156-83111, Iran. Contact e-mail: ahmad_k@cc.iut.ac.ir.

Many attempts have been made by many researchers since 1930 to understand weld residual stresses and distortion using predictive methodology, parametric experiments, or empirical formulations. Attempts have also been made in the last three decades to predict weld residual stresses and distortion through computer simulation of welding process using the finite element (FE) method. Deng and Murakawa (Ref 3) developed two dimensional (2D) and three dimensional (3D) uncoupled thermal-mechanical FE models, based on the ABAQUS software, to simulate the thermal cycles and residual stresses for SUS304 stainless steel pipe. They also developed a thermo-elastic-plastic FE model taking into account the austenite-martensite transformation on the evaluation of residual stress distributions in butt-welded modified 9Cr-1Mo steel pipes (Ref 4). Duranton et al. (Ref 5) performed a 3D modeling of multipass welding of 316L stainless steel pipes, implemented in SYSWELD software. The whole process included 13 weld passes and an adaptive mesh refinement was used in the simulation. Recently, Kermanpur et al. (Ref 6) developed a 3D thermal simulation model based on the FE method in which both surface and volumetric heat flux distributions were considered separately for the gas tungsten arc welding (GTAW) process.

Incoloy 800H is a single phase, austenitic, solid solution alloy with fine dispersion of gamma prime particles and carbides. In general, this alloy has good weldability and all most common processes can be applied to weld it. There is very limited information available on the welding of this material (Ref 7).

In this study, a 3D thermostructural FE model was developed to investigate the temperature and residual stresses distributions in two-pass GTAW process of Incoloy 800H superalloy pipes using the ANSYS commercial software. The FE model was validated against experimental temperature distribution and residual stresses measurements and was used to investigate the welding process.

2. Experimental Procedures

2.1 Welding Experiments

The iron-based Incoloy 800H pipes were circumferentially butt welded. Table 1 shows the chemical composition of Incoloy 800H (Ref 8).

Pipes with outer diameter of 60.3 mm, thickness of 5.54 mm, and length of 80 mm were used. Several single-V groove weld joints were prepared as shown in Fig. 1.

The filler material ERNiCr-3 with chemical composition shown in Table 1 was used. The welding conditions for three samples S1, S2, and S3 with two passes are shown in Table 2.

To prepare correct joints and quality welds, four tack welds were used to maintain the uniform gap of 3 mm. The sequence of tacking and the pass schedules are shown in Fig. 2 and Table 3, respectively.

The pipes were welded in two passes without preheating. To protect the inside face of the first welding pass, one end of two tack-welded pipes was obstructed with a piece of scotch tape and argon inert gas was blown from the other end of the specimen. The ultrasonic inspection tests were carried out to examine the accuracy of the welding experiments.

2.2 Temperature Measurement Tests

To verify the thermal part of the model, temperature measurements were conducted at several points of the pipes in the heat-affected zone (HAZ) with different distance from the welding bead. A personal computer with an integrated PCI-773 measuring card (Eagle Technology) and Lab View 5.1 software was used to record the measured thermal cycles. Figure 3 shows schematic of the test specimen along with the thermocouple locations. Five K-type thermocouples (TC1, TC2, TC3, TC4, and TC5) with diameter 0.3 mm were installed at the locations 3, 7, 11, 15, and 19 mm distance from the groove edge.

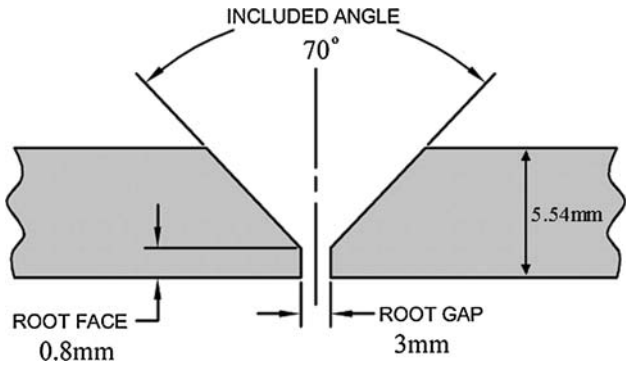

Fig. 1 Geometry of the single-V groove two-pass weld joint design (not to scale)

2.3 Residual Stress Measurement Tests

The residual stresses of the welded pipes were measured using the hole drilling method. Four rosette-type strain gages (SG1, SG2, SG3, and SG4) with 5.13 mm length were installed on the outer surface of the pipes at different distances from the weld line as shown in Fig. 4. The released strains measured were used to calculate the welding residual stresses according to the standard ASTM E837 (Ref 9).

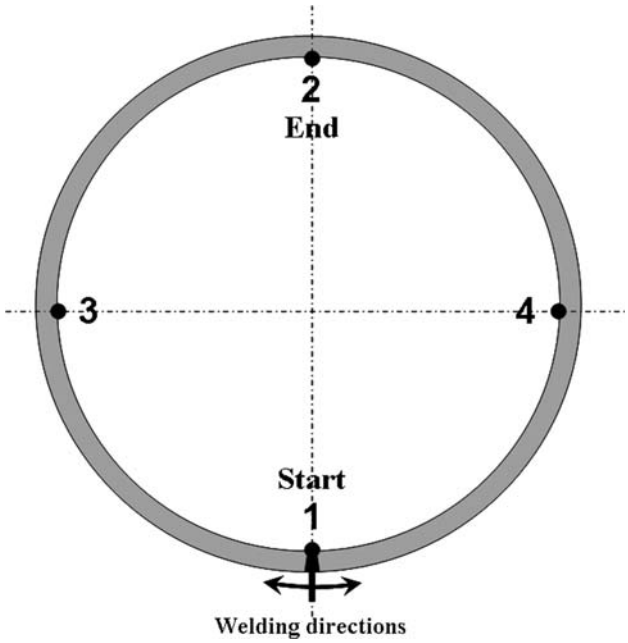

Fig. 2 The sequence of taking and welding directions in experiments

Table 2 The welding conditions of the pipes

Specimen no.	Pass no.	*I*, A	*V*, V	*v*, mm s^{-1}	Net heat input, J mm^{-1}	Polarity
S1	1	80	10	0.77	1038	DCEN
	2	80	10	0.47	1702	DCEN
S2	1	100	10	1.03	970	DCEN
	2	100	10	0.79	1266	DCEN
S3	1	120	10	1.41	851	DCEN
	2	120	10	1.11	1081	DCEN

Table 1 Chemical composition of Incoloy 800H pipes (base) and Inconel 82 (ERNiCr-3 filler material), wt.%

Material	Fe	Ni	Cr	Ti	Al	Mn	Si	Nb	C	S	P
Incoloy 800H	≥39.5	30.0-35.0	19.0-23.0	0.15-0.6(a)	0.15-0.6(a)	≤1.5	≤1.0	···	0.05-0.1	≤0.015	···
Inconel 82	3.0	≥67.0	18.0-22.0	0.75	≤0.3	2.5-3.5	0.5	2.0-3.0	≤0.1	0.015	0.03

(a) %(Al + Ti) = 0.85-1.20

Table 3 The pass sequence parameters used in the welding experiments (H and P stand for half and pass, respectively)

Specimen no.	Pass no.	Welding current, A	Time, s			
			H_1	$H_1 - H_2$	H_2	$P_1 - P_2$
S1	1	80	100	25	100	35
	2		200	25	200	35
S2	1	100	75	25	75	35
	2		120	25	120	35
S3	1	120	55	25	55	35
	2		85	25	85	35

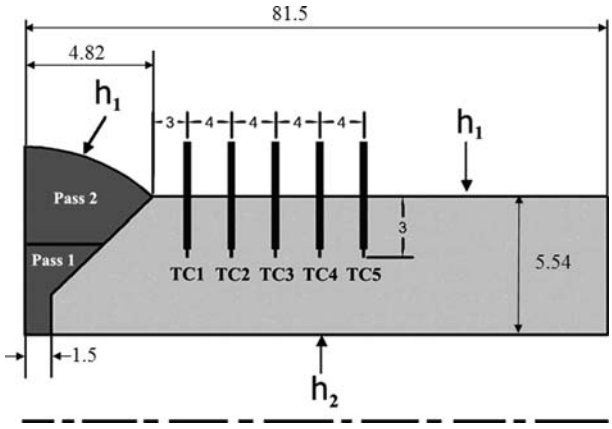

Fig. 3 Schematic of the test specimen along with the thermocouple locations (dimensions in mm but not to scale)

3. Model Theory

3.1 Thermal Model

The spatial and temporal temperature distribution $T(x, y, z, t)$ satisfies the following differential equation for 3D heat conduction:

$$\frac{\partial}{\partial x}\left(k_x \frac{\partial T}{\partial x}\right) + \frac{\partial}{\partial y}\left(k_y \frac{\partial T}{\partial y}\right) + \frac{\partial}{\partial z}\left(k_z \frac{\partial T}{\partial z}\right) + \dot{Q} = \rho C_p \left(\frac{\partial T}{\partial t} - v\frac{\partial T}{\partial x}\right) \quad \text{(Eq 1)}$$

where k_x, k_y, and k_z are thermal conductivity in x, y, and z directions (W m^{-1} K^{-1}), $\dot{Q}$ is the power generation per unit volume in the domain (W m^{-3}), ρ is the density (kg m^{-3}), C_p is the specific heat (J kg^{-1} K^{-1}), and v is the relative velocity of workpiece (here in x direction) (m s^{-1}). The initial condition is:

$$T(x, y, z, 0) = T_0 \quad \text{for } (x, y, z) \quad \text{(Eq 2)}$$

The essential boundary condition is either Dirichlet:

$$T(x, y, z, t) = T_0 \quad \text{(Eq 3)}$$

or natural:

$$k_n \frac{\partial T}{\partial n} - q + h_c(T - T_\infty) + \sigma\varepsilon F\left(T^4 - T_r^4\right) = 0 \quad \text{(Eq 4)}$$

where k_n is thermal conductivity normal to the surface, q is the heat flux (W m^{-2}), h_c is the convective heat transfer coefficient (W m^{-2} K^{-1}), σ is Stefan-Boltzmann constant for radiation (5.67×10^{-8} W m^{-2} K^{-4}), ε is the emissivity, F is the configuration factor, T_∞ is the surrounding temperature, and T_r is the temperature of the radiation heat source. The inclusion of temperature-dependent thermophysical properties along with a radiation term in the above boundary condition makes this type of analysis highly nonlinear. However, the radiation heat exchange can be treated as convection, expressed by the following equivalent heat transfer coefficient:

$$h_r = \sigma\varepsilon F\left(T^2 + T_r^2\right)(T + T_r) \quad \text{(Eq 5)}$$

In this work, a constant equivalent heat transfer coefficient was assigned over the weld bead to treat the radiation boundary condition.

In this analysis, a moving heat source based on the Goldak model was used to apply the heat generated by the torch in the GTAW process. A feature of this model is that a double ellipsoid energy is distributed over a volume described by two ellipsoid regions, one ahead and one after the weld torch. The power density distribution inside the front quadrant becomes (Ref 10):

$$q_f(x, y, z) = \frac{6\sqrt{3}Qf_f}{abc_f\pi\sqrt{\pi}} \exp\left(\frac{-3x^2}{a^2} + \frac{-3y^2}{b^2} + \frac{-3[z + v(\tau - t)]^2}{c_f^2}\right) \quad \text{(Eq 6)}$$

Similarly, for the rear quadrant of the source, the power density distribution inside the ellipsoid becomes:

$$q_r(x, y, z) = \frac{6\sqrt{3}Qf_r}{abc_r\pi\sqrt{\pi}} \exp\left(\frac{-3x^2}{a^2} + \frac{-3y^2}{b^2} + \frac{-3[z + v(\tau - t)]^2}{c_r^2}\right) \quad \text{(Eq 7)}$$

where $Q = \eta VI$ is the total net heat input, η is the arc efficiency that is assumed 0.6 for GTAW process, V is the arc voltage, I is the arc current, v is the welding speed, and τ is the lag factor. The energy deposited in the front and rear quadrants are defined by the fractions f_f and f_r where $f_f + f_r = 2$. Constants a, b, c_f, and c_r are the shape parameters determining the shape and size of the weld pool. The following values were assumed in this investigation: $a = b = c_r = 3$ mm and $c_f = 9$ mm.

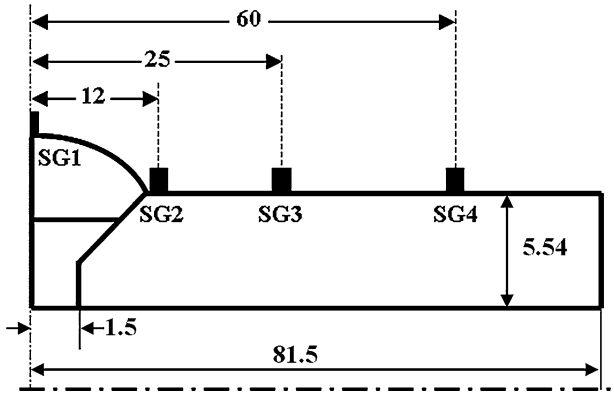

Fig. 4 Schematic of the test specimen along with the strain gage locations (dimensions in mm but not to scale)

3.2 Structural Model

As the solid-state phase transformation does not occur in Incoloy 800H base and the weld metals during the welding process, the total strain rate can be decomposed into three components as follows:

$$\dot{\varepsilon} = \dot{\varepsilon}^{e} + \dot{\varepsilon}^{p} + \dot{\varepsilon}^{th} \quad \text{(Eq 8)}$$

where the first, second, and third terms in the right side represent elastic, plastic, and thermal contributions, respectively. The elastic strain is modeled using the isotropic Hook's law with temperature-dependent Young's modulus and Poisson's ratio. The plastic behavior of the material was described by Von Mises yield function and bilinear kinematics hardening was assumed. The kinematics hardening is taken into account as an important feature because material points typically undergo both loading and unloading in course of the welding process. Finally, the thermal strain is computed using the temperature-dependent coefficient of thermal expansion (Ref 3).

4. Numerical Simulation

The GTAW process was simulated with the FE method using the ANSYS commercial code (Ref 11). Due to symmetry, only half of the welded pipes were modeled. In this work, a sequentially coupled physics analysis was used to link the thermal and structural fields by applying the thermal results to the structural model as loads. The simulation parameters for the both models are described below.

4.1 Thermal Part

The 20-node 3D thermal element SOLID90 with a single degree of freedom (temperature) was used for the bulk material (both the base and weld zones). The FE mesh is shown in Fig. 5 consisting of 4704 elements.

This mesh was based on a mesh sensitivity analysis performed for several mesh refinements. The maximum temperature of the pipe achieved during the welding process was considered as the basis of the sensitivity analysis. Figure 6 shows a plateau in the maximum temperature after the element number 4704. This mesh shown by an arrow in Fig. 6 was then considered for simulations to get mesh-independent results with a reasonable CPU time.

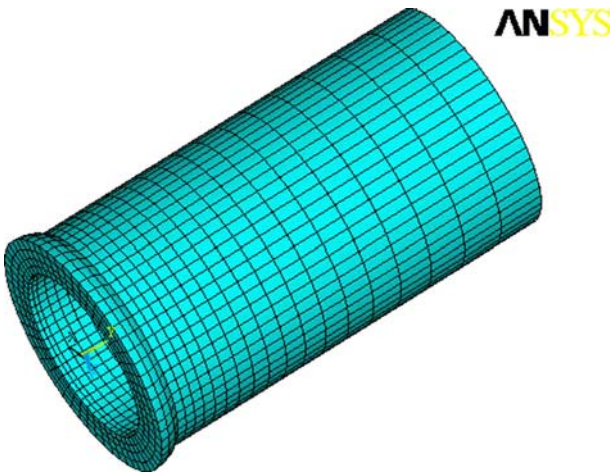

Fig. 5 The finite element mesh of the pipe

It was assumed that the GTAW torch is attached to the origin of the moving coordinate system. The coordinate system was therefore translated through the discretized domain based on the welding speed and the mesh size in a discontinuous manner. The element birth and death technique was used to simulate the weld filler material variation with time in the multipass butt-welded joints (Ref 11). All elements must be created, including those weld fillers to be born in later stages of the analysis. The method deactivates these elements by multiplying their stiffness by a severe reduction factor (e.g., 10^{-6}). Although zeroed out of the load vector, element loads associated with deactivated elements still appear in element-load list. Similarly, mass, damping, specific heat, and other such effects are set to zero for deactivated elements. The mass and energy of deactivated elements are excluded from the summations of the model. When elements are born, they are not actually added to the model, but are simply reactivated: its stiffness mass, element loads, etc. return to their full original values.

To take into account the effect of thermal convection within the weld pool, thermal conductivity of the alloy above the solidus temperature was fictitiously increased by the order of 2 (Ref 12). The boundary conditions allow for both convection and radiation. Radiation losses are dominating for higher temperatures near the weld and convection losses for lower temperatures away from the arc. A combined boundary condition was used here, which accounts for both convection and radiation. The resulting expression for the temperature-dependent heat transfer coefficient h_1 is given by Eq 9 (Ref 13):

$$\begin{aligned} h_1 &= 0.0668T\ (\mathrm{W\,m^{-2}\,K^{-1}}) \quad 0 < T < 500\,^{\circ}\mathrm{C} \\ h_1 &= 0.231T - 82.1\ (\mathrm{W\,m^{-2}\,K^{-1}}) \quad 500\,^{\circ}\mathrm{C} < T \end{aligned} \quad \text{(Eq 9)}$$

The boundary condition expressed by Eq 9 was applied for all outside free boundaries of the pipe including the successive boundaries created for each new weld pass. For the inside free boundaries, because of the blowing argon gas, the constant value $h_2 = 20$ ($\mathrm{W\ m^{-2}\ K^{-1}}$) was assumed. The temperature-dependent thermophysical properties of the Incoloy 800H used in the simulation are shown in Fig. 7 (Ref 14).

4.2 Structural Part

The 20-node 3D structural element SOLID95 with three degrees of freedom (three displacement components) was used

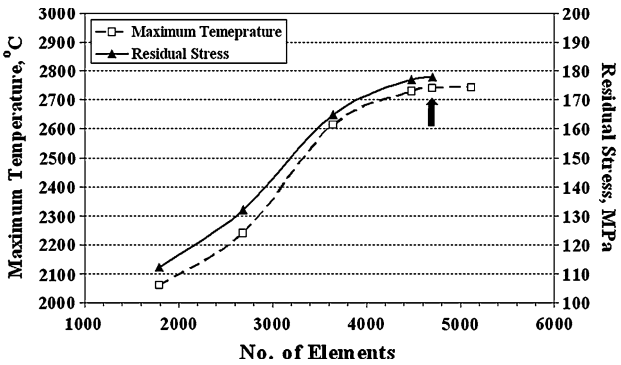

Fig. 6 Mesh sensitivity analysis for both thermal and structural models based on the maximum temperature of the pipe

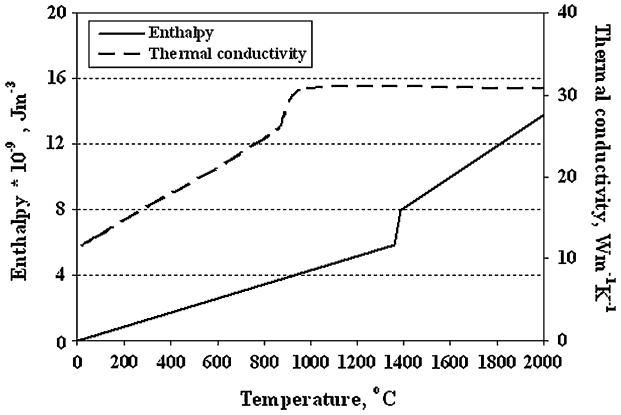

Fig. 7 Physical properties of the Incoloy 800H alloy as a function of temperature used in the thermal model

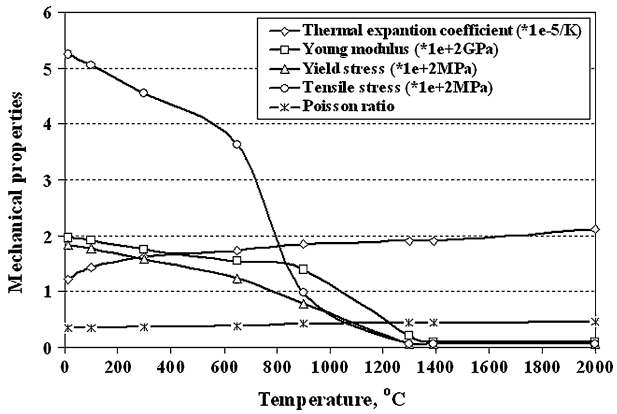

Fig. 8 Mechanical properties of the Incoloy 800H alloy as a function of temperature used in the structural model

for the bulk material (both the base and weld zones). The FE mesh consists of 4704 element as shown in Fig. 5. The mesh sensitivity analysis for the structural model is shown in Fig. 6 showing the mesh used for the simulations. Temperature-dependent mechanical properties of Incoloy 800H are shown in Fig. 8.

The boundary conditions for the structural model are shown in Fig. 9. In the weld zone, thermal strains are computed for newly activated elements based on the current load step temperature and the reference temperature, T_{REF}, as follow:

$$\varepsilon^{th} = \alpha(T)(T - T_{REF}) \quad \text{(Eq 10)}$$

where T is the element evaluation temperature, T_{REF} is the temperature at which zero thermal strain exists, and $\alpha(T)$ is the temperature-dependent thermal expansion. To specify material-dependent reference temperature, the material property REFT can be used instead of the global T_{REF}, specifying the activation temperature as a stress-free temperature. This temperature is called softening temperature at which the Young's modulus and the yield stress of the material are so low that the new element can be applied without any stresses. When the element temperature is greater than the material's softening temperature, there will be no elastic strain or total strain in the element until the element cools to the softening temperature (Ref 11, 13).

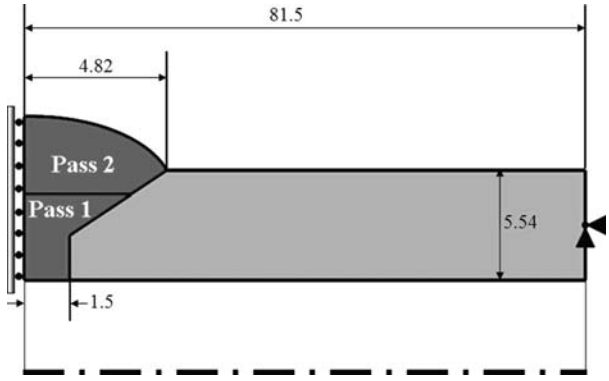

Fig. 9 The boundary conditions for the structural analysis

5. Results and Discussion

5.1 Experimental Validation of the Simulation Model

The present simulation model was validated against the experimentally measured temperature distribution and residual stresses. Figure 10 compares the experimental thermal cycles of different thermocouples with the corresponding simulation results for the sample S2 showing a good agreement.

Figure 11 shows the residual axial stresses curve on the outside surface of the pipe for the sample S1. As it can be seen, there is also a good agreement between the simulation results and experimental values. The differences between the results are believed to be due to the additional residual stresses created during drilling, resulting in an over-estimation in the measured residual stresses compared to the simulated predictions. However, the general trend of the experimental values is accurately simulated by the model.

5.2 Prediction of Residual Stress Distributions

Figure 12 shows distribution of residual axial stresses against normalized distance, x/t, on the symmetry plane of the model for sample S1, in which x is distance from the inside of pipe to outside and t is the pipe thickness. It can be said that due to the low pipe thickness and a higher heat input of the second pass than the first one, almost both inside and outside surfaces of the pipe undergo the same thermal cycle during the second welding pass (Ref 13). Therefore, the circumferential shrinkage of the pipe resulted from the second pass is not constrained by the first one. The straight dash line shown in Fig. 12 is the distribution of the residual axial stresses through the thickness, recommended by the ASME XI Task Group for piping flaw evaluation, which is valid for $t \leq 25$ mm (Ref 15). The present result is therefore in agreement to this recommendation.

Figure 13 shows contour of residual axial stresses on the symmetry plane of the model at the weld centerline of sample S1. According to this figure, a tension-compression distribution of the axial stresses can be seen through the thickness from the inside to the outside surface of the pipe. It can also be seen that at the start and end of each half pass, the axial stresses are slightly different from the other locations.

As shown in Fig. 14, a circumferential shrinkage takes places during welding that causes inward deformation of the weldment and its vicinity. This deformation, well known as the

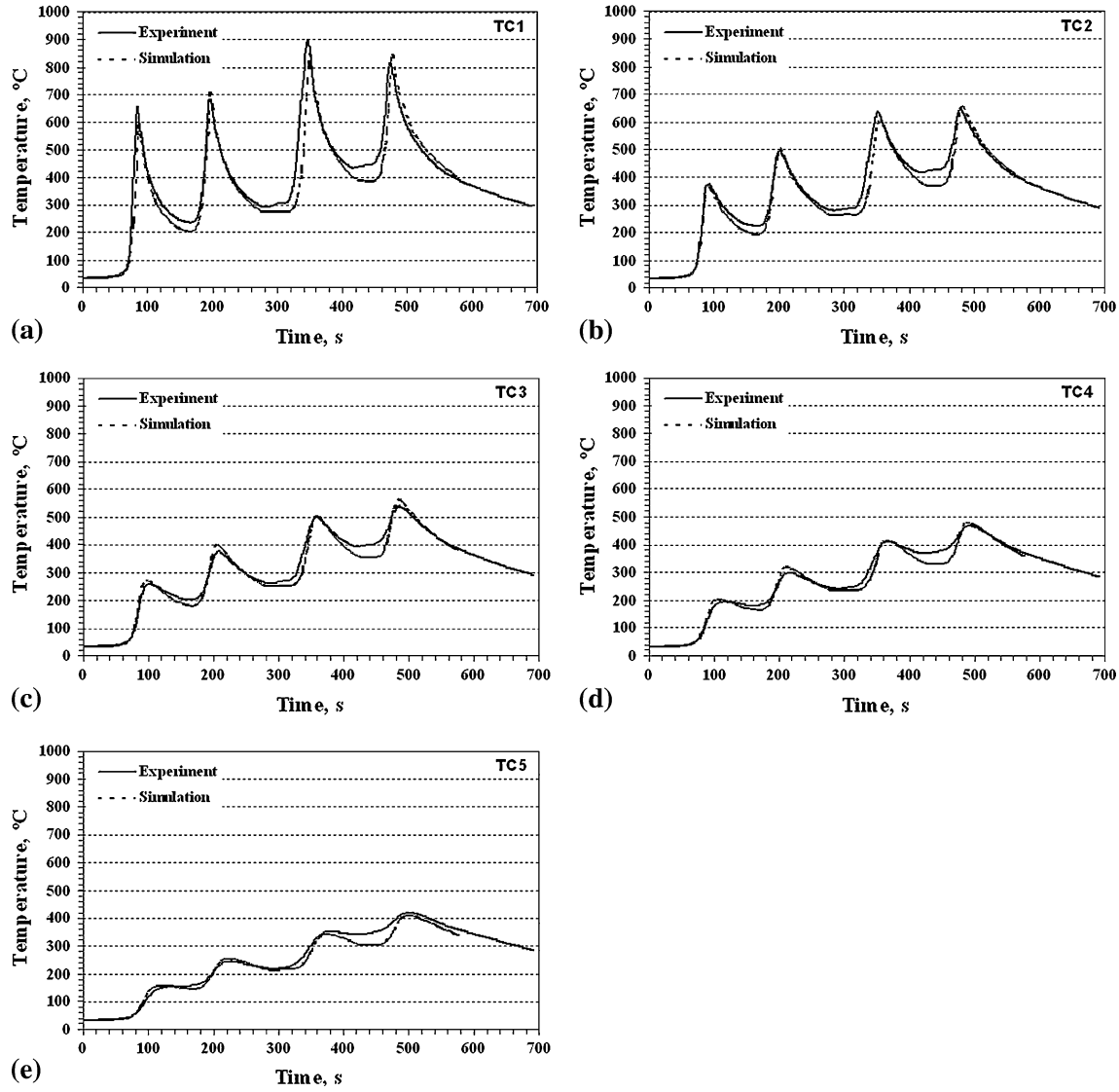

Fig. 10 Comparison between the experimental thermal cycles for different thermocouples with the corresponding simulation results for sample S2: (a) TC1, (b) TC2, (c) TC3, (d) TC4, and (e) TC5

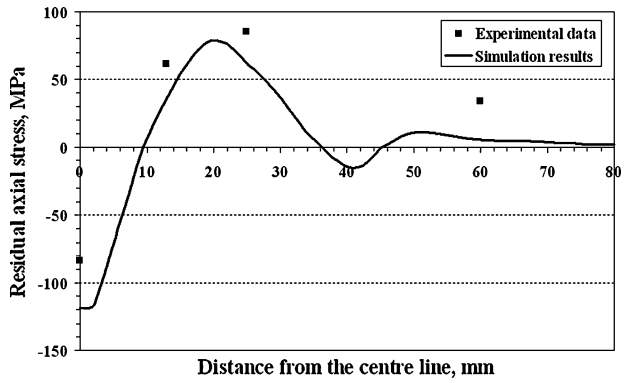

Fig. 11 Comparison between the experimental residual stress with the corresponding simulation results for sample S1

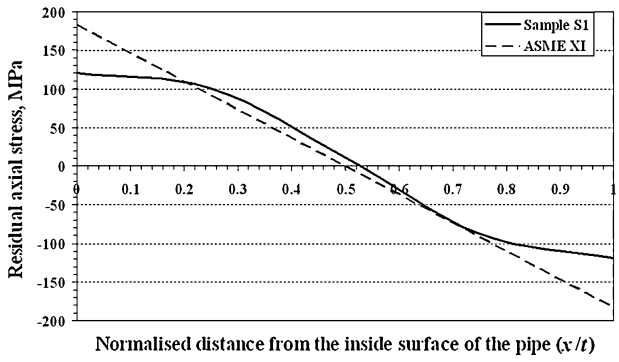

Fig. 12 Distribution of residual axial stresses against normalized distance, *x*/*t*, on the symmetry plane of the model for sample S1

"tourniquet effect," will cause tensile stresses on the inside surface and compression stresses on the outside surface of the pipe.

The residual hoop stresses were determined by the axial stresses and yield strength of the metal. Figure 15 shows distribution of the residual hoop stresses against the normalized

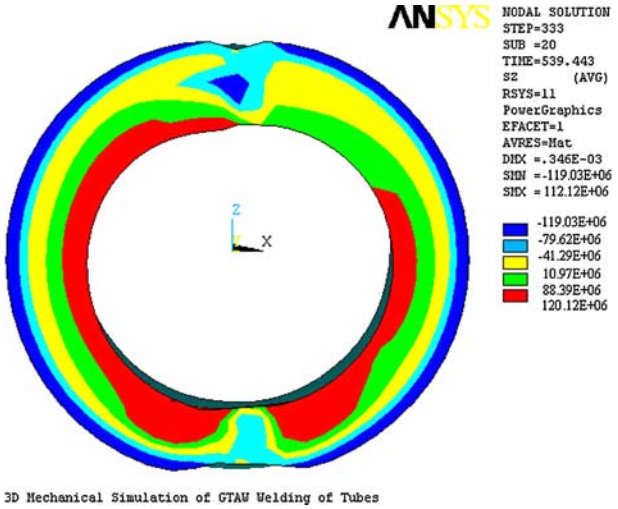

Fig. 13 Contours of residual axial stresses on the symmetry plane of the model at the weld centerline of sample S1

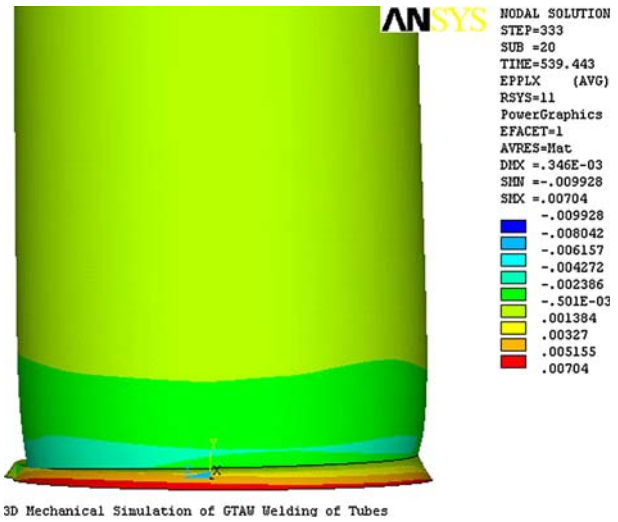

Fig. 14 The "tourniquet effect" in the two-pass circumferential butt GTAW process of pipes

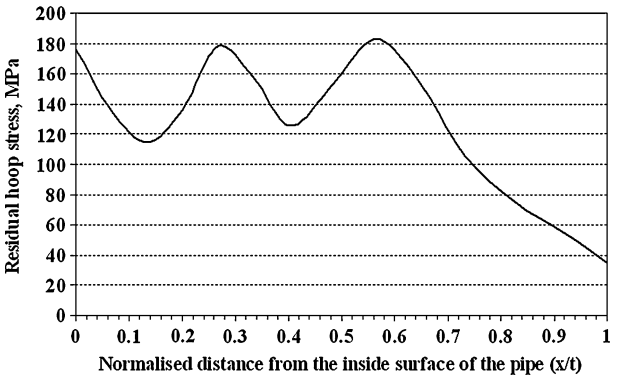

Fig. 15 Distribution of residual hoop stresses against the normalized distance on the symmetry plane of the model for sample S1

distance on the symmetry plane of the model for sample S1. As can be seen, the hoop stresses have a tensile distribution through the thickness but decrease from the inside to the outside surface of the pipe as a result of the compression axial stress. Figure 16 shows contour of the residual hoop stresses on the symmetry plane of the model for sample S1.

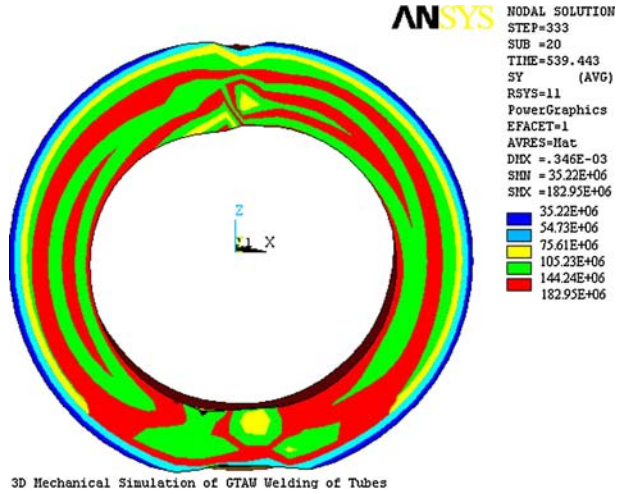

Fig. 16 Contours of residual hoop stresses on the symmetry plane of the model for sample S1

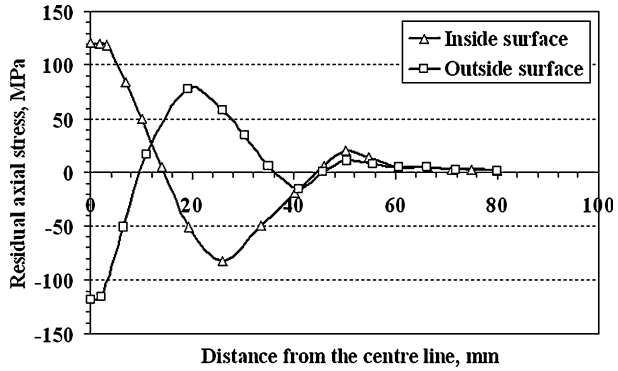

Fig. 17 Residual axial stresses distribution through the axial direction of the pipe S1 at the inside and outside surfaces

Figure 17 shows the residual axial stresses distribution through the axial direction of the pipe S1 at the inside and outside surfaces, respectively. As can be seen, the residual axial stress in the weld zone is tensile for the inside surface and compressive for the outside. Both stresses approach to zero with the increasing distance from the centerline such that in the HAZ their contributions become vice versa. As expected, the residual stresses approach to zero in the distance far from the weld bead.

5.3 Effect of Heat Input on Residual Stresses

Residual stresses in axial direction have a great effect on flaws in the butt welding. Axial stresses are directly related to initiation and propagation of the fatigue cracks and stress corrosion cracking (Ref 13, 16, 17). The process parameters affecting the axial stresses are therefore important for process engineers. One of the most important parameters is the heat input. Figure 18 shows distribution of residual axial stresses against normalized distance, *x/t*, on the symmetry plane of the model for three samples with different heat inputs (as listed in

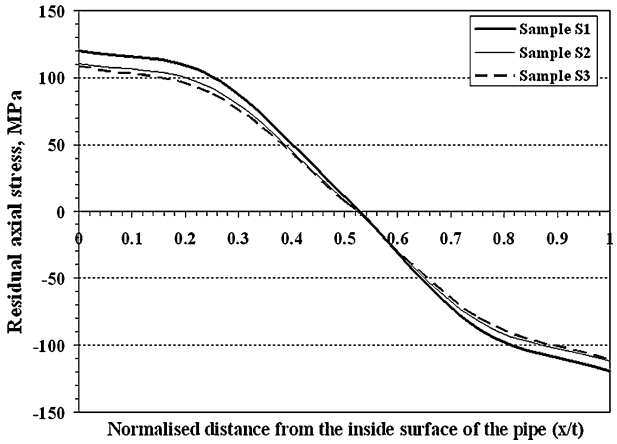

Fig. 18 Distribution of residual axial stresses against normalized distance, *x/t*, on the symmetry plane of the model for three samples with different heat inputs

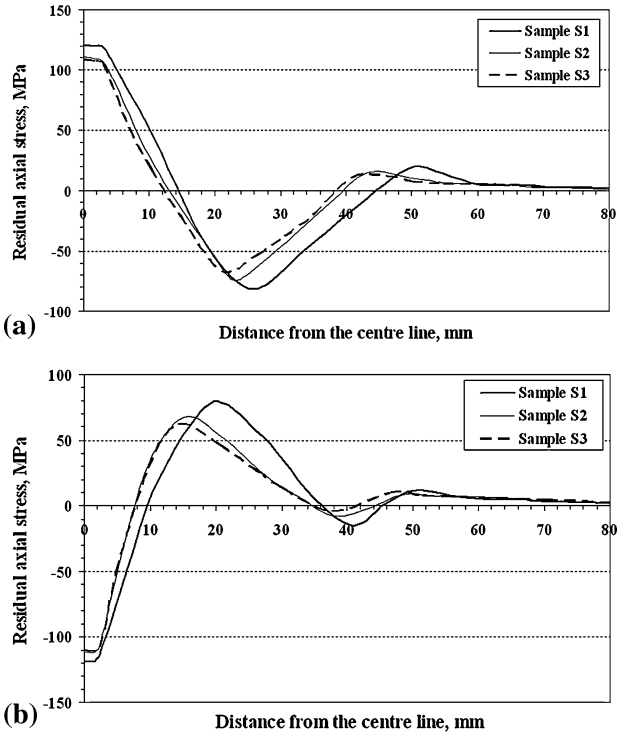

Fig. 19 Distribution of residual axial stresses through the axial direction of the pipes S1, S2, and S3 at the (a) inside and (b) outside surfaces

Table 3). It is shown that sample S1 has greater tensile axial stresses on the inside surface and compressive axial stresses on the outside surface compared to the other samples. This is because the sample S1 was welded under the higher heat input in the second pass than others. The heat input in the second pass for the samples S2 and S3 are almost the same, thereby having the similar residual stresses. As the allowable size of defects such as cracks corresponds to the residual axial stresses, it can be said that the sample S1 could have larger defects than the other samples.

Figure 19(a) and (b) shows distribution of the residual axial stresses through the axial direction of the pipes S1, S2, and S3 at the inside and outside surfaces, respectively. As can be seen, the sample S1 with the higher heat input in the second pass shows higher tensile and compressive residual axial stresses in the inside and outside surfaces compared to the other samples. This is in agreement with the residual axial stress distribution through the pipe thickness (as shown in Fig. 18).

6. Conclusions

A 3D decoupled thermostructural FE model was developed for circumferential butt GTAW process of Incoloy 800H pipes. The validated model against experimental observations of temperature and residual stress fields showed that the tensile residual axial stresses were developed on the inside surface of the pipe within the weld zone which gradually converted to the compressive type in the HAZ. The residual axial stresses developed on the outside surface of the pipe were opposite to the inside surface. The model also showed the direct effect of the heat input on the development of residual axial stresses during the GTAW of the pipes. The present model is a proper tool for control and optimizing distribution of residual stresses in petrochemical pipes during welding.

Acknowledgments

The authors would like to acknowledge the Oil Refinery Company of Isfahan, Iran for their partial financial support and permission for publishing the paper and also Dr. E. Heshmat Dehkordi for his invaluable support and assistance in the residual stress measurements.

References

1. K. Masubuchi, *Analysis of Welded Structures*, Pergamon Press, New York, 1980
2. Sh. Sarkani, V. Tritchkov, and G. Michaelov, Efficient Approach for Computing Residual Stresses in Welded Joints, *Finite Element Anal. Des.*, 2000, **35**, p 247–268
3. D. Deng and H. Murakawa, Numerical Simulation of Temperature Field and Residual Stress in Multi-Pass Welds in Stainless Steel Pipe and Comparison with Experimental Measurements, *Comput. Mater. Sci.*, 2006, **37**, p 269–277
4. D. Dean and M. Hidekazu, Prediction of Welding Residual Stress in Multi-Pass Butt-Welded Modified 9Cr-1Mo Steel Pipe Considering Phase Transformation Effects, *Comput. Mater. Sci.*, 2006, **37**, p 209–219
5. P. Duranton, J. Devaux, V. Robin, P. Gilles, and J.M. Bergheau, 3D Modelling of Multipass Welding of a 316L Stainless Steel Pipe, *J. Mater. Process. Technol.*, 2004, **153–154**, p 457–463
6. A. Kermanpur, M. Shamanian, and V. Esfahani Yeganeh, Three-Dimensional Thermal Simulation and Experimental Investigation of GTAW Circumferentially Butt-Welded Incoloy 800 Pipes, *J. Mater. Process. Technol.*, 2008, **199**, p 295–303
7. L. Sundar and D.R.G. Achar, Review of the Weldability of Incoloy Alloy 800, *Indian Weld. J.*, 1998, **8**, p 134–142
8. "Specification for Nickel-Iron-Chromium Alloy Seamless Pipe and Tube." ASTM B407-87/ASME SB407, 2008, 8 pp
9. *Metals Test Method and Analytical Procedures*, Vol. 03.02, ASTM International, West Conshohocken, 2005, E837
10. J. Goldak, A. Chakravarti, and M. Bibby, New Finite Element Model for Welding Heat Sources, *Metall. Trans. B*, 1984, **15**, p 299–305
11. *ANSYS User's Manual, Version 10*, Swanson Analysis Systems, Inc., Houston, 2006

12. S.Y. Lee and S.J. Na, Numerical Analysis of Molten Pool Convection Considering Geometric Parameters of Cathode and Anode, *Weld. J.*, 1997, **76**, p 484s–497s
13. B. Brickstad and B.L. Josefson, Parametric Study of Residual Stresses in Multi-Pass Butt-Welded Stainless Steel Pipes, *Int. J. Press. Vessel. Pip.*, 1998, **75**, p 11–25
14. G.H. Little and A.G. Kamtekar, Effect of Thermal Properties and Weld Efficiency on Transient Temperatures During Welding, *Comput. Struct.*, 1998, **68**, p 157–165
15. ASME Section XI, Task Group for Piping Flaw Evaluation Pressure Vessel and Piping Codes, *ASME J. Press. Vessel. Technol.*, 1986, **108**, p 352–366
16. M. Law, H. Prask, V. Luzin, and T. Gnaeupel-Hrold, Residual Stress Measurements in Coil, Linepipe and Girth Welded Pipe, *Mater. Sci. Eng. A*, 2006, **437**, p 60–63
17. C.C. Silva and J.P. Farias, Non-Uniformity of Residual Stress Profiles in Butt-Welded Pipes in Manual Arc Welding, *J. Mater. Process. Technol.*, 2008, **199**, p 452–455